Photoreduced graphene oxide recovers graphene hot electron cooling dynamics

Alden N. Bradley,[1,*] Spencer G. Thorp,[1,*] Gina Mayonado,[1] Sergiu A. Coporan,[2] Edward Elliott,[2] and Matt W. Graham[1,†]
[1]*Department of Physics, Oregon State University, Corvallis, Oregon, 97331, USA*
[2]*Voxtel Nano, Corvallis, Oregon, 97330, USA*

(Received 27 February 2023; revised 9 May 2023; accepted 30 May 2023; published 16 June 2023)

Reduced graphene oxide (rGO) is a bulk-processable quasiamorphous two-dimensional material with broad spectral coverage and fast electronic response. rGO sheets are suspended in a polymer matrix and sequentially photoreduced to measure the optical absorption and ultrafast hot-electron cooling dynamics. Photoreduced graphene oxide (GO) yields absorption spectra that fit the same Fano line shape parameters as monolayer (ml) graphene. With increasing photoreduction time, rGO transient absorption kinetics reach an optimal point that matches the hot-electron cooling dynamics simultaneously measured in ml-graphene. After each stepwise photoreduction, the rGO ultrafast kinetics are simulated with the hot-electron cooling model of graphene that is mediated by disorder-assisted supercollisions. The hot-electron cooling rate of moderately photoreduced GO is 0.31 ps^{-1} and closely matches the ml-graphene result. Subsequent photoreduction increases the disorder parameter associated with the hot-election cooling, consistent with an order of magnitude smaller mean-free scattering length from photoionized point defects. GO photoreduction yields increasing photoluminescence from localized graphene quantum dot (GQDs) and decreasing 2.3 eV emission from oxygenated defect-edge states. By pumping localized GQD states and probing graphene, a 0.17 ps delayed rise-time emerges that accelerates with photoreduction, suggesting an energy transfer process.

DOI: 10.1103/PhysRevB.107.224309

I. INTRODUCTION

Graphene oxides (GOs) are widely used substitutes for the remarkable mechanical properties of graphene, but their highly amorphous lattice lacks desirable electronic properties such as high conductivity, fast photoresponse, and broad spectral coverage. When GO is incorporated in certain polymeric networks, we show that systematic photoreduction makes it more graphenelike while maintaining the pristine optical-quality of the films. GO has oxygenated functional groups attached to the two-dimensional (2D) carbon lattice via out-of-plane bonds that prevent GO sheets from aggregating in the solution phase [1,2]. GO can be made more graphenelike by chemical or photothermal reduction resulting in reduced GO (rGO). Conventionally, these graphenelike rGO layers aggregate and scatter light strongly, making their optical properties hard to compare against monolayer (ml)-graphene. Using systematic reduction of isolated GO-in polymer composites, we show the emergence of spectral line shapes and extract ultrafast hot-electron cooling dynamics that are closely analogous to that of ml-graphene.

GO is often used as a bulk-processable substitute for graphene for wide-ranging applications, including electronic sensing, plasmonics, and desalination [3–9]. The large presence of oxygen in GO introduces an effective band gap [Fig. 1(a) inset], with a tunable energy determined by the carbon-to-oxygen ratio. Previous theoretical and experimental studies suggest band gaps ranging from ∼0.6 to 3.1 eV for GO that can vanish nearly completely as GO is reduced [10]. GO samples reduced via pulsed Xe arc lamps effectively remove hydroxyl, epoxy, and carboxyl groups to increase the size of graphenelike sp^2 regions. The amount of photoreduction changes the ratio of the oxygenated-sp^3 to conjugated-sp^2 sublattice regions [11–13]. Very selective growths and controlled reduction are required to realize desired optoelectronic applications for GO that have included broadband optical nonlinearity [14,15], tunable photoluminescence (PL) [16], and resonant energy transfer [17].

With widely varying ratios of oxygen and carbon, the highly inhomogeneous and amorphous nature of GO and rGO lattices make a direct comparison with ml-graphene difficult. In rGO, individual sp^2 graphenelike sublattice regions often become surrounded by sp^3 oxidized domains, forming molecularlike confined regions often called graphene quantum dots (GQDs) or graphene nanoclusters. While the composition of rGO varies greatly, it can roughly be decomposed into three types of sublattices illustrated in Fig. 1(b): (1) extended sp^2 hybridized regions, (2) confined sp^2 lattice nanoclusters or GQDs, and (3) oxidized or sp^3 regions. Zhang *et al.* [18] performed transient absorption (TA) on rGO in solution and found that the carbon (sp^2) and oxidized domains (sp^3) could be treated independently [19]. Photoexcited carriers in the spatially confined sp^2 GQDs produce Frenkel excitons with energies tunable with the size of the GQD conjugation network [20,21]. The local oxygenated functional groups at domain edges also create many optically active defect states within the lattice that are seen in PL studies [22–24].

While some of the mechanical and chemical properties of GO-based materials are analogous to graphene, the conditions necessary to replicate graphenelike electronic behavior in rGO

*These authors contributed equally to this paper.
†graham@physics.oregonstate.edu

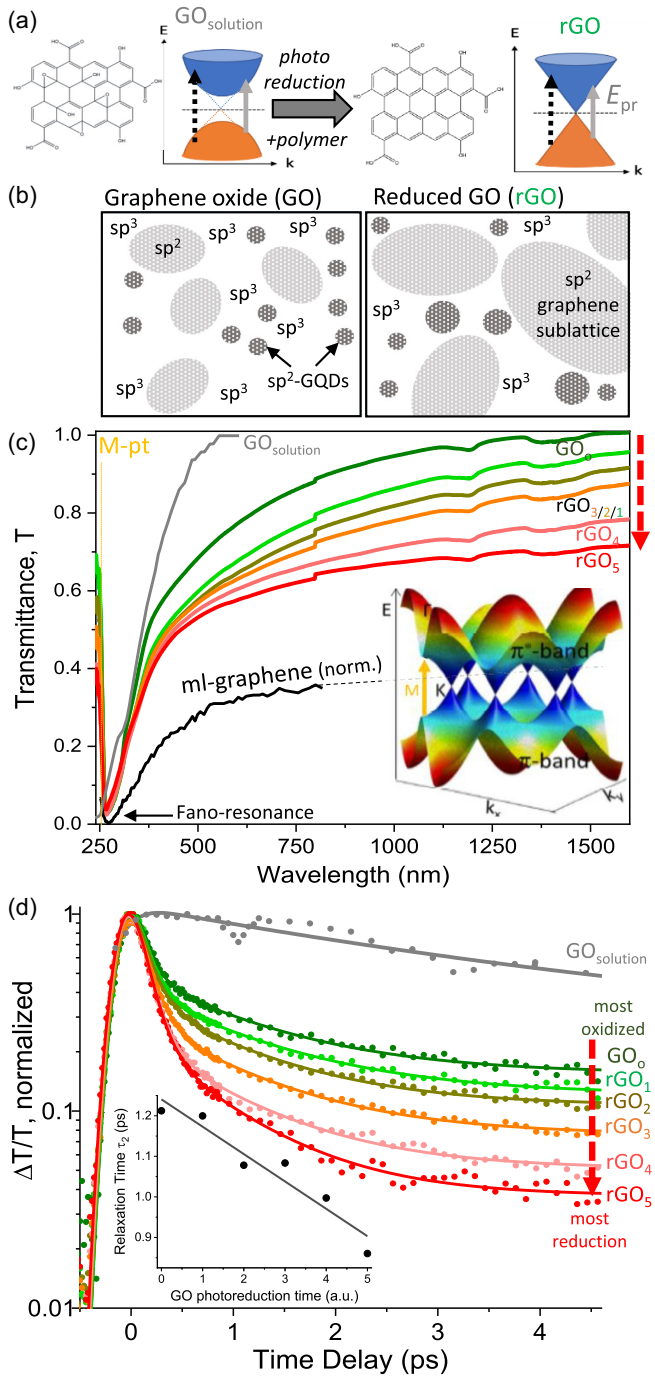

FIG. 1. (a) Comparison of graphene oxide (GO) vs. reduced GO (rGO) band and chemical structures. (b) Illustration of the three prominent sublattice types within the rGO structure [sp^2, sp^2 graphene quantum dot (GQD), and oxygenated sp^3 lattice]. (c) Linear absorption spectra are measured at five stages of the photoreduction. With increasing photoreduction, near-infrared (NIR) transmittance decreases to more closely approximate the (renormalized) chemical vapor deposition (CVD) monolayer (ml)-graphene transmittance curve. Conversely, as-grown GO in solution (gray line) has a prominent π-π^* band gap. (inset) Graphene band structure highlighting the M–saddle point transition. (d) Corresponding transient transmittance kinetics at $E_{\text{probe}} = 1.8$ eV show carrier relaxation accelerates with reduction. (inset) The τ_2 lifetime increases linearly with photoreduction.

are less clear. Past studies have compared the TA response of GO and rGO prepared by chemical reduction in solution [25–27] and thin films [24,28]. This paper concerns the optical properties of GO and rGO embedded in a transparent polymer film over six controlled degrees of photoreduction. The TA relaxation resolves how the ultrafast hot-electron cooling rate is modified at each stage of photoreduction using tunable probe energies ranging from 1.2 to 2.3 eV, while the hot-electron cooling in graphene is typically modeled with two rates associated with optical phonon scattering and disorder-assisted relaxation processes [29–31]. In addition to graphenelike relaxation, prior rGO studies are dominated by a long 10–200 ps relaxation component previously ascribed to electron trapping at defect sites [26,32].

The results obtained from the successive photoreduction of GO are modeled with first-principles models of absorption line shapes and hot-electron cooling applied previously to graphene. In Sec. IV A, the evolution of the absorption line shape with photoreduction is modeled by competing contributions from graphenelike Fano lineshape and GO-oxide-related absorption. Then Sec. IV B applies a hot-electron supercollision (SC) model to determine at what stage of photoreduction rGO most closely matches the dynamics of ml-graphene. Over most visible and ultraviolet (UV) excitation energies, Sec. IV C shows the GO sublattice and GQD states dominate both the PL and ultrafast response. Lastly, we resolve how photoreduction of GO impacts the ultrafast rate of energy transfer from the photoexcited GQDs to graphene acceptor states.

II. EXPERIMENTAL METHODS

The GO and rGO polymer samples were fabricated using commercially available chemically exfoliated GO sheets (Graphenea) containing ∼53% carbon and ∼44% oxygen. The sheets are dispersed in a N, N-dimethylacrylamide (DMAA) polymer with added PMMA sites to scaffold the GO and minimize aggregation. To remove all solvent, the mixture is cured between two 1-mm-thick glass slides, resulting in a sample thickness of 200 μm. The sample is then photoreduced via a pulsed xenon arc lamp at a 1-Hz repetition rate. This low frequency was chosen to prevent gas bubbles from forming during the reduction process. Absorbance is measured via a Cary IR-UV-Vis spectrometer. Both excitation and emission PL are detected with a commercial fluorimeter (Horiba NanoLog).

Both degenerate and nondegenerate pump-probe experiments are conducted with 140 fs pulses from a Ti: Sapphire lasers (Coherent Chameleon) and Optical Parametric Oscillators (APE OPO Compact). An optical parametric amplifier is used to tune the output wavelength. The beam is split into two parts: A strong pump and a weaker probe power beam with a ratio of ∼10:1. The intensity of the pump beam is modulated using an acousto-optic modulator (AOM, Crystal Tech) at 500 kHz. The polarizations of the pump and probe beams are linear and set parallel to each other. For the nondegenerate experiment, the pump beam is frequency doubled by a second harmonic generation unit (OPE SHG) prior to modulation. Additionally, a white-light supercontinuum is generated (NKT Photonics FemtoWHITE800 fiber

module) and selectively filtered (ThorLabs 10 nm bandpass) to provide a broadly tunable probe for ml-graphene and select rGO transient transmittance data. Both beams are focused onto the sample by a single lens. The probe beam waist at the sample is $\sim$80 μm. The transmitted probe beam is detected by a thermoelectrically cooled InGaAs photodiode lock-in amplification (Zurich Instruments, HFLI and MFLI) at 500-kHz modulation.

To compare the rGO polymer physics with ml-graphene, similar measurements to the above were carried out using an ultrafast TA microscopy setup with a 1 μm spot size. The ml-graphene was prepared by chemical vapor deposition (CVD) and wet-transferred to a thin silicon nitride grid. The above nondegenerate pump-probe scheme was used in a collinear geometry coupled to a 4*f*-confocal scanning microscope (Olympus BX51W). The absorption spectra of ml-graphene are taken on the same microscope by coupling in a tunable Xe-arc illumination source and detecting the full plane images on a camera (EMCCD, PI-ProEM) after background renormalization.

III. RESULTS

Spanning the UV to NIR regions, Fig. 1(c) plots the absolute linear transmission of six GO samples in a polymer composite with increasing photothermal reduction times labeled from rGO_1 to rGO_5. Additionally plotted on a renormalized scale, we overlay the linear absorption spectra of both pristine ml-graphene (black line) and the starting as-grown commercial GO solution (gray line, $GO_{solution}$). The GO solution has a clear band gap, peaking at the molecular π-π^* transition. Conversely, ml-graphene gives an expected Fano resonance line shape peaked at 265 nm, redshifted from the *M*–saddle-point transition labeled in Fig. 1(c) (inset) [33]. The rGO_0 curve in Fig. 1(c) is the as-grown GO after incorporation into a hybrid polyacrylic and PMMA polymer matrix described in the methods. The absolute absorbance increases monotonically with GO photothermal reduction time over the NIR and IR regions plotted (from 0.35 to 1.5 eV). Photoreduction of GO leads to a spectral line shape that absorbs light more analogously to CVD ml-graphene plotted in Fig. 1(c).

PMMA is required to transfer graphene from the Cu growth foil to the substrate (Si_3N_4 in our case). It is nearly impossible to remove all PMMA polymer residue from CVD graphene (except by the harshest plasma treatments). After transfer to the silicon nitride substrate, the spun-cast PMMA layer is removed by successive acetone and isopropyl alcohol washes. While partial PMMA polymer removal is required to make ohmic electrical contacts to graphene, it does not modulate the NIR TA kinetics [34]. Due to the required transfer off of the Cu growth foil, PMMA polymer is present (in varying concentrations) in nearly every publication using CVD ml-graphene. By using PMMA microspheres to scaffold and prevent aggregation of the rGO sheets, we show some advantageous electronic physics of ml-graphene can be extended to bulk phase processing.

In the solution phase and most polymers, GO aggregates as it is reduced, resulting in colloidal mixtures that strongly scatter light. GO is incorporated in a polymer-sphere matrix scaffold that makes systematic photoreduction possible while maintaining pristine optical quality films. Thus, we can compare the absorption line shapes, PL, and ultrafast hot-electron cooling rates over a wide range of photoreduction. Interestingly, the more heavily reduced GO samples in Fig. 1(c) have a transmittance line shape and slope similar to ml-graphene throughout the NIR regions. In the graphenelike regions accessible with our NIR probe energy, the local chemical and dielectric environment of the PMMA polymer microsphere is not expected to change appreciably with photoreduction. This is supported by carefully monitoring absorption and fluorescence spectra plotted in Figs. 1(c), 3, 5(a), and S2 and S3 in the Supplemental Material [35] at each reduction stage. In Fig. S2 in the Supplemental Material [35], the rGO absorbance is plotted out to 3000 nm, and no evolution of new peaks is observed. The lack of new spectral peaks or enhanced scattering background suggests photothermal reduction is not altering the PMMA environment where rGO resides.

Figure 1(d) plots the normalized transient transmission ($\Delta T/T$, semilog scale) kinetics of sequentially photoreduced GO/rGO samples acquired with a 1.8 eV degenerate pump and probe configuration. As the degree of reduction increases, the kinetic relaxation rate accelerates. The data shown in both Figs. 1 and 2 fit (solid lines) to a least-squares algorithm requiring three exponents (τ_1, τ_2, and τ_3) with pulse deconvolution for the 155 fs laser autocorrelation response. After GO is incorporated and stabilized in the polymer matrix, the relaxation dynamics accelerate monotonically with photoreduction time. In stark contrast, the as-grown solution of GO [gray line in Fig. 1(d)] has much longer TA relaxation dynamics at all time scales, bearing little resemblance to faster graphene.

At a 1.8 eV visible probe energy, the GO polymer composite that received no reduction (highest oxygen content) has the longest TA relaxation kinetics with its τ_3 component comprising 21% of total decay amplitude. The inset of Fig. 1(d) shows the τ_2 lifetimes all decrease linearly from $\sim$1.2 to 0.9 ps with increasing lamp photoreduction time. All samples have a characteristic τ_2 time similar to the characteristic $\sim$1 ps decay of graphene expected for the 1.8 eV probe, suggesting all five samples exhibit graphene-like hot-electron cooling dynamics. By analogy with ml-graphene, τ_1 would be associated with relaxation by optical phonons and τ_2 with disorder-assisted hot-electron cooling [31]. The longest τ_3 lifetime was $>\sim$30 ps but beyond that of data taken for all photoreductions. All other fitting parameters are shown in Figs. 2(c) and 2(d).

Figure 2 plots how the kinetic relaxation rates depend on the selected probe energy (E_{probe}). Comparing Fig. 2(a) at $E_{probe} = 1.3$ eV to Fig. 1(d) at 1.8 eV, a similar pattern with photoreduction emerges. However, the longest component τ_3 is negligible for all five cases of photothermal reduction $rGO_{1–5}$. In Fig. 2(d), the slower τ_2 lifetime decreases linearly from 2.5 to 1 ps with increasing photoreduction time. Here, τ_1 varies the least with photoreduction. Interestingly, the most reduced samples relax even faster than CVD-grown ml-graphene (black dashed line). Figure 2(a) shows fits to a triexponential decay curve with lifetimes of $\sim$0.4 ps and 1–2.5 ps for τ_1 and τ_2, respectively.

Regardless of the incident TA probe energy (1.2–1.8 eV), rGO samples relaxed progressively faster as the photoreduction time increased. Figure 2(b) shows that TA dynamics of

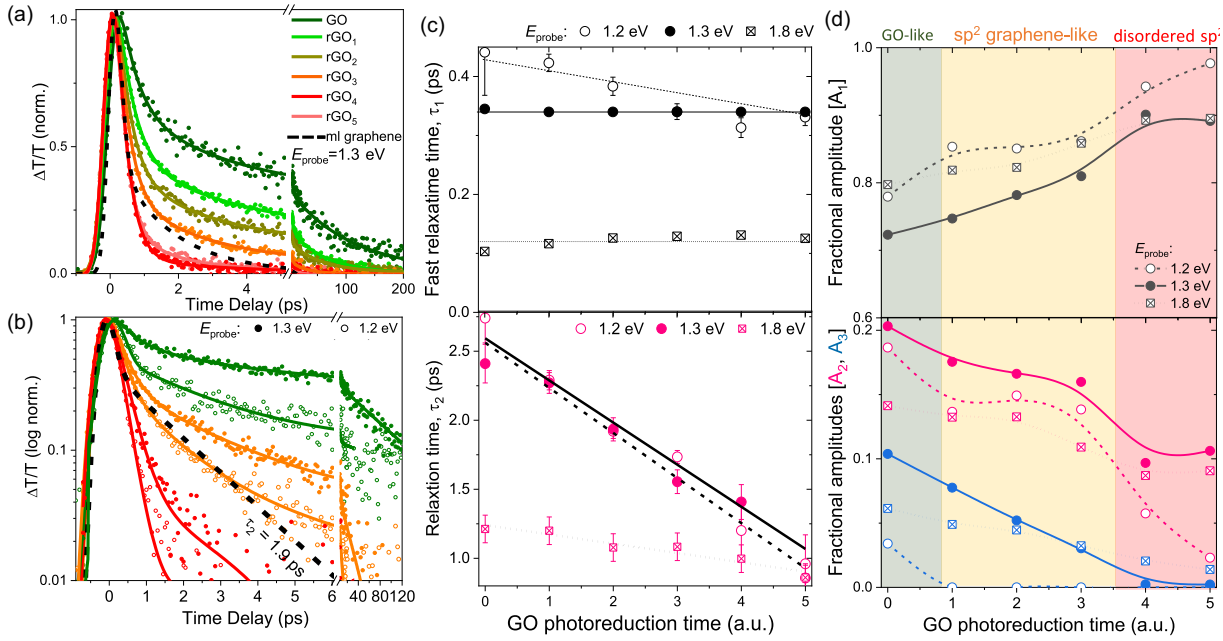

FIG. 2. (a) $\Delta T/T$ relaxation kinetics at $E_{\text{probe}} = 1.3$ eV accelerate with sequential graphene oxide (GO) photoreduction. Fits show two exponential lifetimes, with only the most oxidized samples requiring a third lifetime of $\tau_3 = 61 \pm 2$ ps. (b) The $\Delta T/T$ kinetics for $E_{\text{probe}} = 1.2$ eV (open circles) relax faster than at 1.3 eV (closed circles). The rGO_3 photoreduction stage most closely approximates the monolayer (ml)-graphene interband relaxation kinetics shown (dashed line). (c) For each probe energy, the τ_1 lifetimes (top) are roughly constant, whereas the τ_2 lifetime (bottom) decreases linearly $\sim 2.5\times$ during which photoreduction becomes even faster than ml-graphene. (d) Amplitudes ($A_{1/2/3}$) of each lifetime component suggest a composition change with increasing amplitude from sp^2 sublattice dynamics. The smallest A_3 (blue) amplitude quickly decreases to zero as GO is reduced.

GO, rGO_3, and rGO_5 are slower at $E_{\text{probe}} = 1.3$ eV (closed circles, 2.6 eV pump) than the $E_{\text{probe}} = 1.2$ eV (open circles, 2.2 eV pump) probe energy window. Interestingly, the most reduced sample rGO_5 always decays more quickly than ml-graphene. This faster decay relative to graphene suggests that the photothermal reduction is ultimately damaging the sp^2 graphene sublattice by causing increased disorder and defect sites. These low-energy disorder states have been previously observed in conjugated carbon systems [36,37]. This is further supported by the qualitative increase in lattice defect states that is evident by increased emission in the IR region of the PL spectra (see Fig. S2 in the Supplemental Material [35]).

Figures 2(c) and 2(d) contain the results of our exponential fitting lines shown in Figs. 1(d) and 2(a) and 2(b) (solid lines). The top panel shows the amplitude of the fast time component ($\sim$0.4 ps) at 1.2, 1.3, and 1.8 eV, which accelerates only moderately as the GO samples are reduced. The bottom panel of Fig. 2(c) shows the τ_2 relaxation time of GO decreases roughly linearly with photoreduction time. At all probe energies, the τ_2 relaxation time decreases with reduction, with $rGO_{3,4,5}$ having lifetimes shorter than that of CVD graphene under the same optical conditions. The CVD ml-graphene (dashed line in Figs. 1 and 2) was fit to a $\tau_2 = 1.9$ ps at 1.2 eV and 1.1 ps at 1.8 eV probe energies, respectively.

In most heavily oxygenated rGO samples, the longest $\tau_3 \sim 61$ ps component comprises up to 16% of the total decay amplitude. Such samples contain many functional groups; however, the large band gap of the fully oxidized regions is well outside the spectral range of both pump and probe laser energies. Instead, GQDs create gapped sp^2 moleculelike regions with size-tunable band gaps that are resonant with our probe beam [22]. For $rGO_{3,4,5}$ samples, Fig. 2(d) shows that the τ_3 time component is zero for $E_{\text{probe}} < 1.3$ eV, suggesting only graphenelike sp^2 sublattice regions are relevant to the electronic dynamics throughout this NIR probe region.

IV. ANALYSIS AND DISCUSSION

A. Reduced graphene oxide Fano line shape absorption analysis

The transmission spectra in Figs. 1(a) and S2 in the Supplemental Material [35] and fitted absorption spectra in Fig. 3 all show line shapes similar to ml-graphene throughout the NIR and IR spectral regions from $\sim$0.4 to 3.5 eV. The absorption maxima of both ml-graphene and rGO in Fig. 3 (black line) deviate from the tight-binding model prediction of the graphene van Hove singularity M-point resonance at $\sim$5.1 eV [38]. Instead, the graphene absorption is best fit by a Fano line shape with a renormalized peak resonance energy E_r that is redshifted from the M point energy by $\cong$0.3–0.4 eV [39,40]. The asymmetric Fano line shape accounts for the ratio of interference between the discrete (M-point) and continuum transition probabilities through the dimensionless Fano parameter q [39]. Thus, the tight-binding model of the graphene absorption spectrum in Fig. 3 is renormalized for effective electron-hole interaction effects by fitting to the below asymmetric Fano line shape:

$$A_{\text{Fano}}(E) = A\left\{\frac{\left[\frac{2}{\gamma}(E - E_r) + q\right]^2}{1 + \left[\frac{2}{\gamma}(E - E_r)\right]^2}\right\}, \tag{1}$$

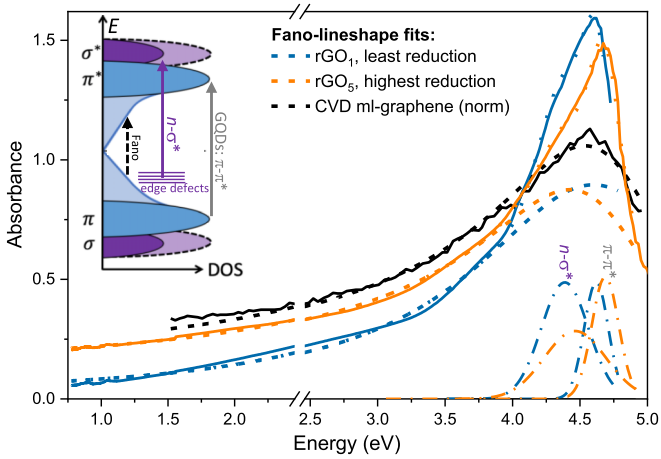

FIG. 3. Under each linear absorption spectra (solid lines) the separated Fano resonance line shape fit is plotted in dashed lines. Unlike pristine monolayer (ml)-graphene (black), the two reduced graphene oxide (rGO) samples plotted also require two summed Gaussians (dash-dot), suggesting molecularlike transitions labeled π-π^* and edge-defect transitions, n–σ^* (see inset). The resulting summation of the Fano-Gaussian fits (dotted lines) show the graphene sublattice Fano parameter, q increases with photoreduction consistent with more lattice disorder.

where γ is the Lorentzian homogeneous linewidth, and A is the amplitude scaling constant. Figure 3 plots a spectral measurement of CVD ml-graphene (black line) with its corresponding Fano line shape fit (dashed line), given by Eq. (1) above. Table I gives the resulting Fano parameters and the shows good agreement of the graphene values in this paper with the established literature values [39,41]. This provides an essential calibration base to quantitatively compare against the line shape fit of rGO absorption spectra.

Figure 3 spectral fitting shows good agreement between the absorption spectra of rGO_1 and rGO_5 and the asymmetric Fano resonance after it is summed with two Gaussian peaks at energies corresponding to the absorption of the n-σ^* and π-π^* transitions. This fitting analysis suggests that the absorption spectrum in rGO can be understood to contain a Fano resonance similar to that of CVD ml-graphene. The molecularlike π-π^* transitions are illustrated in Fig. 3 (inset) and show GQD states also contribute to the spectral weight and are centered near 4.6 eV [42]. At 4.3 eV, rGO also contains subgap defect states between the π and π^* states, which result from a previously reported local oxygen-based disorder that creates edge defect state (n)-to-σ^* transitions [2,43–46]. Due to the heterogeneous oxygen coverage, these local disorder edge states have a much broader absorption full width at half maximum (FWHM). As rGO_1 is further reduced, we observe in Fig. 3 that the peak area of the n-σ^* Gaussian decreases as oxygen is removed, resulting in fewer edge states. Both our most oxidized samples (GO_0 and $GO_{solution}$) did not fit well to a Fano line shape, suggesting only rGO samples have a graphenelike absorption line shape in the IR and NIR regions.

TABLE I. Fano fitting parameters for data in Fig. 3 (dashed lines) show good agreement with our ml-graphene data and established literature values [39,40]. The Fano parameter q of rGO_5 best matches ml-graphene. A Gaussian peak for the localized GQD π-π^* and π-σ^* edge sate transitions are also required.

Sample	E_r (eV)	γ (eV)	q
ml-graphene (CVD)	4.80	1.69	−3.2
ml-graphene (exfoliated) [39]	4.73	1.30	−3.3
rGO_5 (highest reduction)	4.69	1.68	−3.2
rGO_1 (least reduction)	4.62	2.16	−50

Table I contains a summary of the Fano fitting parameters, showing good agreement between the literature [39,41] and our results for ml-graphene and rGO_5. Here, rGO_5 contains a large absorption from the linear dispersion near the K and K' points, where excited carriers couple strongly to the continuum, similar to ml-graphene. For rGO_1, the Fano parameter q decreases significantly from ml-graphene, suggesting electron-hole interaction effects are increasingly screened for transitions near the van Hove singularity. For GO and lightly reduced GO, Table I shows the Fano parameter is many times larger than highly reduced samples and ml-graphene. This suggests the many edge states in more oxidized graphene couple strongly to continuumlike states.

The inset of Fig. 3 shows a qualitative depiction of how the density of states changes from GO to rGO. As the samples are reduced, they contain larger area regions of noninterrupted sp^2 carbon, leading to a more graphenelike distribution of continuum states, resulting in a better Fano line shape fit. The two summed Gaussians show the effect of reduction on the absorption spectra, with the amplitude of the n-σ^* transition decreasing significantly, suggesting the removal of oxygen functional groups. We also see that the absorption peak in rGO_1 shifts slightly to lower energy compared with rGO_5. This shift has been theoretically predicted by Roy *et al.* [22], who used density functional theory (DFT) to calculate the band structure of GO at varying oxygen content, finding that the addition of oxygen decreases the band gap at the M point. However, the underlying Fano resonance energy (E_R in Table I) does not change with photoreduction. The very large Fano parameter q required to fit the most oxidized rGO_1 samples suggests the sp^2 hybridized regions are not extensively delocalized and retain a molecularlike character.

B. Hot-electron cooling rates in reduced graphene oxide

Figure 4 fits the hot-electron cooling TA kinetics in progressively reduced GO as the TA probe energy is decreased from 1.3 eV (top) to 1.2 eV (bottom). Specifically, the hot-electron cooling rate (τ_{SC}) is extracted. Unlike the exponential rate τ_2 from Fig. 2, τ_{SC} is analogous to the recombination rate as the electrons cool near the Fermi energy and is independent of probe energy (E_{probe}). To connect the above phenomenological exponential relaxation model of rGO to this first-principles hot-electron cooling model, the TA relaxation kinetics fits in Fig. 4 instead use the hot-electron heat dissipation rate $H = C_e(dT_e/dt)$, where C_e and T_e are the electronic heat capacity and temperature, respectively. Figure 4(a) contains the first-principles hot-electron cooling model fits (solid lines) to the normalized TA kinetics of the rGO samples. Hot-electron cooling rates in rGO can be qualitatively

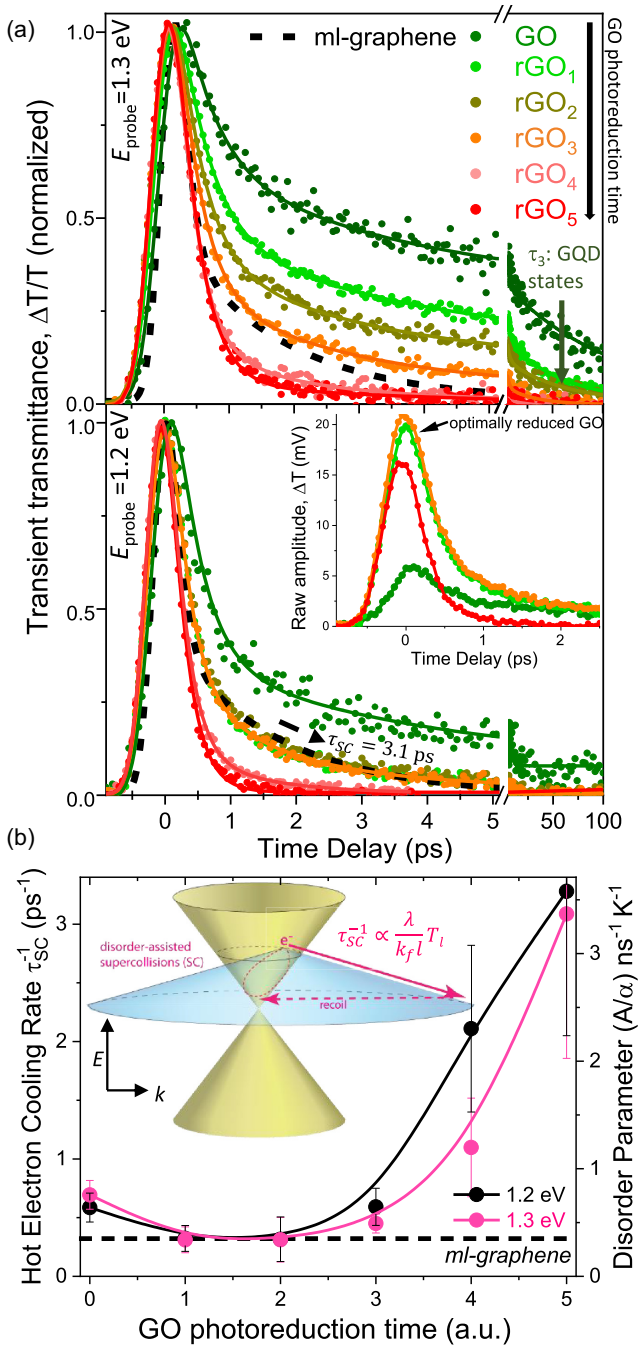

FIG. 4. (a) Transient absorption (TA) relaxation kinetics of the six progressively reduced graphene oxide (GO) films are plotted against monolayer (ml)-graphene (black dashed) at probe energies of 1.3 eV (top) and 1.2 eV (bottom). Fitted lines extract the supercollision (SC) hot-electron cooling rates of graphene, τ_{SC}^{-1}. (inset) The corresponding raw signal amplitude ΔT grows ~4× as the total graphenelike area coverage increases, going from GO (dark green) to rGO_{1-3}. Subsequent photoreduction (red) reverses this trend, decreasing both TA amplitude and τ_{SC}. (b) τ_{SC}^{-1} electronic cooling rates of GO thin films are plotted with increasing photoreduction time. For moderately reduced samples (rGO_{1-3}), the SC model electron cooling disorder parameter $A/\alpha \cong (3\tau_{SC}T_l)^{-1}$ is similar to the ml-graphene rate (dashed) at both probe energies. (inset) Schematic of the disorder-assisted SC hot-electron cooling model of graphene [31,47] mechanism that is applied to rGO.

understood by comparing with CVD ml-graphene kinetics (black dotted line). The lowest-energy probe ($E_{probe} = 1.2$ eV) in the bottom panel of Fig. 4(a) shows the hot-electron cooling rate response of ml-graphene (dashed line) is identical to rGO_1, rGO_2, and rGO_3.

The inset of Fig. 4(a) (lower panel) shows the raw TA amplitude signal ΔT also tunes nonmonotonically. With stepwise photoreduction, this amplitude first quickly increases ~4×, consistent with the percent area of graphenelike regions in rGO growing. As photoreduction continues, ΔT reverses direction and decreases moderately to suggest increasing graphene lattice disorder. This general amplitude trend mirrors the hot-electron cooling rate (τ_{SC}^{-1}) trend in Fig. 4(b), offering secondary evidence of the emergence of graphenelike electronic cooling in rGO. With stepwise photoreduction, this amplitude first quickly grows ~4×, suggesting the percent area of sp^2 graphene is growing. Afterward, ΔT decreases moderately, consistent with increasing graphene lattice disorder. This general amplitude trend mirrors the hot-electron cooling rate (τ_{SC}^{-1}) plotted in Fig. 4(b) and provides secondary confirmation of the emergence of graphenelike electronic cooling in rGO. Interestingly, $rGO_{4,5}$ dissipates heat even faster than CVD ml-graphene.

The mechanism for fast energy dissipation or hot-electron cooling in graphene has been widely debated in the past. The optical phonon dissipation model [30,48,49] evolves on the subpicosecond relaxation time scale of the τ_1 component. At longer relaxation times, the disorder-mediated acoustic phonon decay pathway or SC hot-electron cooling model is the primary factor limiting cooling of the photoexcited hot-electron temperature $T_e(t)$ [50]. Experimental studies demonstrate the SC model [50] successfully predicts the photocurrent [31] and optical [51,52] and electrical [47] heating response of graphene. However, the applicability of the SC model to the more disordered lattice of GO and rGO has not been considered.

To understand hot-electron cooling in rGO, we apply the disorder-assisted acoustic phonon SC model. Illustrated in Fig. 4(b) (inset), hot electrons preferentially cool by scattering off-grain boundaries and lattice disorder to enable more energetic acoustic phonons (see pink arrows) to dissipate heat far more efficiently than would otherwise occur if acoustic phonon scattering was restricted to 2D band structure (yellow cone). In the SC model, hot-electron cooling near the Fermi level occurs without crystal momentum conservation. Instead, higher-energy ($\sim k_B T_e$) acoustic phonons are emitted with the momentum imbalance q_{recoil} accounted for by disorder-induced intrinsic lattice recoil [50]. This SC hot-electron model is illustrated in Fig. 4(b) (inset) and accelerates the cooling rate of the hot-electron temperature T_e defined by [31,50]

$$\frac{dT_e}{dt} = -\frac{H}{\alpha T_e} = -\frac{A}{\alpha}\frac{T_e^3 - T_l^3}{T_e}, \tag{2}$$

where A/α is the SC rate coefficient, and T_l and T_e are the lattice and electron temperatures, respectively. Solving Eq. (2), $T_e(t) \cong \frac{T_o}{1+AT_o t/\alpha}$ when $T_e(t) \gg T_l$, where T_o is the initial electron temperature. Since all data shown are at $T_l = 292$ K, the transient change in $T_e(t)$ is small compared with T_l, or

$T_e(t) - T_l \ll T_l$ such that we can approximate Eq. (2) by expanding the leading terms to arrive at the room-temperature hot-electron temperature $T_e(t) \cong T_l + (T_o - T_l)\exp(-t/\tau_{SC})$, to get the expression $\tau_{SC}^{-1} = 3AT_l/\alpha$ [31].

The TA response is obtained using the hot-electron (or hole) temperature (T_e) through analytically fitting to the transient interband optical conductivity $\Delta\sigma(E_{probe}, t) = -e^2/4\hbar\{f_{e/h}[T_e(t), E_{probe}] - f_{e/h}(T_l, E_{probe})\}$ [38]. The Fermi-Dirac hot-electron occupancy function $f_{e/h}[T_e(t), E_{probe}]$ at the probe energy (E_{probe}) equations are given in the Supplemental Material [35] as a change in interband optical conductivity $\Delta\sigma(t, E_{probe})$ [38,52]. In Fig. 4(b), the hot-electron cooling rates (τ_{SC}^{-1}) for rGO are extracted by fitting the data in Fig. 4(a) to the analytical SC-model solution [Eq. (2)], allowing for two additional exponential components (τ_1 and τ_3). This fast component $\tau_1 \cong 0.34$ ps averages over the initial electron thermalization and optic phonon emission time scale and is discussed elsewhere [53,54]. Any molecularlike π-π^* transitions present are captured by the 1.2 and 1.3 eV probe-energy long time component $\tau_3 \sim 61$ ps.

The accelerating TA relaxation kinetics in Fig. 4(a) are consistent with the idea that photoreduction of GO creates more disorder and defects in the graphene sublattice. Figure 4(b) shows an increase in the rate of hot-electron cooling τ_{SC}^{-1}. Unlike the earlier exponential fits, the rate τ_{SC}^{-1} is independent of the probe energy and is the rate at which the hot-electron Fermi-Dirac distribution cools [51]. The hot-electron cooling time for the comparison ml-CVD -grown graphene [dashed line in Fig. 4(b)] at 292 K is 3.1 ps. Here, τ_{SC}^{-1} increases by a factor of ~6 as the samples are reduced. This suggests the xenon arc lamp used to reduce GO is a largely destructive process to the underlying sp^2 sublattice. At the highest level of photoreduction, Fig. 4(b) suggests the increased lattice disorder destroys the desired graphenelike extended lattice by creating too many point defects.

Photoinduced defects (disorder) accelerate the hot-electron relaxation rate in ml-graphene. For rGO samples 2 and 3, this SC graphene-based hot-electron cooling model yields similar optical phonon-assisted cooling (τ_1) and acoustic-phonon SC cooling times (τ_{SC}). By showing that optimally reduced GO transient transmittance matches ml-graphene, Fig. 4(a) suggests the graphenelike lattice may be largely decoupled from the coexisting localized GQD or oxide sites. This demonstration of graphene photophysics in bulk-processable rGO suggests new scalable modalities to better harness desirable electronic properties of graphene.

For ml-graphene, Song *et al.* [50] derived the SC hot-electron relaxation rate $\tau_{SC}^{-1} = 3AT_l/\alpha$ which provides a direct measure of lattice disorder through the expression:

$$\frac{A}{\alpha} \cong \frac{2}{3}\frac{\lambda}{k_F l}\frac{k_B}{\hbar}, \tag{3}$$

where the mean-free scattering path is $k_F l$. The electron-phonon coupling strength can be approximated as $\lambda = \frac{D^2}{\rho s^2}\frac{2E_F}{\pi(\hbar v_F)^2}$, where both the deformation potential D and Fermi energy E_F are experimental variables that serve to increase the hot-electron cooling rate. Figure 4(b) shows that $\frac{A}{\alpha} \cong 0.3$ ns^{-1}K^{-1} for rGO_{1-3}, which matches the ml-CVD graphene values in the literature [51]. However, further photoreduction increases $\frac{A}{\alpha}$ by $\sim 10\times$, suggesting the graphene sublattice is being damaged. If the deformation potential is approximately constant, then $A/\alpha \propto E_F/k_F l$, suggesting that the damage from photoreduction decreases the mean-free scattering path by photoionization, which increases sp^2 sublattice defect sites. Our fitted data in Fig. 4 confirm that the disorder-assisted acoustic phonon SC model best describes the rate-limiting heat dissipation kinetics for rGO data. Figure 4(b) shows how photodamage-induced disorder is likely shrinking $k_F l$ scattering length to accelerate the rGO lattice hot-electron cooling rate. The inset of Fig. 4(a) (lower panel) also shows a similar nonmonotonic trend for the raw transient transmittance signal for rGO, $\Delta T(t) \sim \Delta V(t)$ in mV from the lock-in amplifier ($E_{probe} = 1.2$ eV). The amplitude trend of each $\Delta T(t)$ curve is opposite to the τ_{SC}^{-1} trend in Fig. 4(b). Further photoreduction decreases both τ_{SC} and the total transient transmittance in Figs. 4(a) (inset) and S5 in the Supplemental Material [35], consistent with an increase in the point-defect density and a smaller k_Fl length. Collectively, the matching nonmonotonic trends in amplitude and τ_{SC}^{-1} suggest optimal photoreduction occurs for rGO_{2-3}, where the rGO films exhibit the most graphenelike properties. This stepwise photoreduction employed lattice disorder controllably, providing new evidence of the disorder-assisted SC electron cooling model for graphene.

C. Oxygenated sublattice contributions from graphene quantum dots

Sections IV A and IV B both show the rGO sample and ml-graphene have remarkably similar line shapes and hot-electron cooling rates over optical energies that range from 0.4 to 1.8 eV. This section focuses on the differences that arise in visible and UV ranges where GQDs and defect-edge states can also be optically excited. Figure 5(a) plots the PL emission spectra of the least reduced GO_0 and most reduced rGO_5 samples after a 4.6 eV excitation. The main asymmetric peak appears to shift from ~2.4 to 2.7 eV with photoreduction. The experimental emission spectra (dots) are fit (solid lines) using four summed Gaussian peaks (dotted lines). All peak energies and FWHM spectral widths (except at 2.34 eV) are found to be approximately invariant to photoreduction. The peak at 2.7 eV in Fig. 5(a) corresponds with emission from the smallest GQD state (labeled GQD_1) π^*-π orbital relaxation. At lower energies, both peaks centered ~1.55 and 1.80 eV grow with photoreduction, consistent with emission from larger GQD states labeled GQD_2 and GQD_3, respectively. We observe an increase in the emission intensity from these three sp^2 peaks with reduction, confirming they do not result from oxygen groups. Conversely, the emission at 2.3 eV represents the carrier recombination in sp^3 oxygen (σ^*-n). The magnitude and width of this emission decrease with reduction as oxygen functional groups are removed. PL from GO and rGO in solution has been widely documented in the literature, showing that reduction of GO increases PL intensity at NIR wavelengths while also blueshifting the main peak [42,55,56]. In agreement, Fig. 5(a) shows an increase in PL intensity with reduction at peaks centered at 1.80 and 1.55 eV. The PL of the oxygenated GO lattice is known to emit broadly ~2.4 eV with locally varying oxygen content responsible for

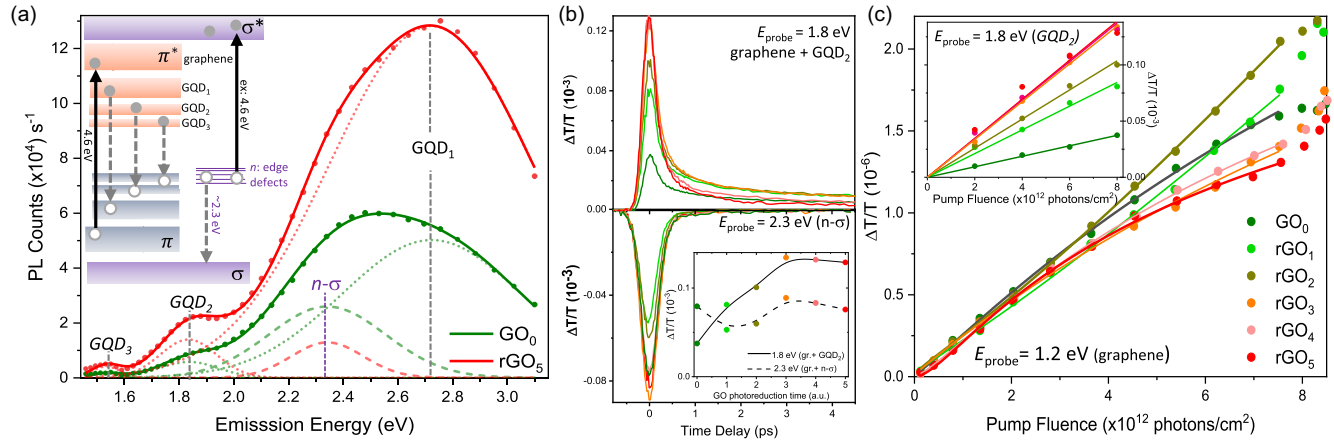

FIG. 5. (a) The photoluminescence (PL) emission spectra of GO_o (green line fit) and rGO_5 (red line fit) with the four constituent Gaussians of the fit (dashed lines). Photoreduction increases the PL peaks from graphene quantum dot resonances, labeled GQD_{1-3}. Conversely, emission from the oxygenated sublattice $n-\sigma$ defect edge states decreases as graphene oxide (GO) is reduced (see inset for corresponding transitions). (b) The degenerate TA response near the 1.8 eV GQD_2 resonance (top) vs near the excited state absorption at 2.3 eV (bottom). Probe fluences are $\sim 8 \times 10^{12}$ photons/cm^2 and $\sim 32 \times 10^{12}$ photons/cm^2 for top and bottom, respectively. (inset) Transient absorption (TA) response increases with photoreduction. (c) $\Delta T/T$ pump power photon fluence dependence of reduced GO samples using a 1.2 eV probe. Fits are to the graphene supercollision (SC) hot-electron cooling model in Eq. (2). Over a wide range of incident photon flux, the saturable absorption susceptibility $\Delta T/T$ is invariant to photoreduction, suggesting only graphene hot electrons are probed below $\sim$1.2 eV. (inset) Conversely, at 1.8 eV, $\Delta T/T$ changes strongly, suggesting increasing GQD_2 states.

the broader FWHM [28,45]. In rGO, PL is dominated by π^*-π carrier recombination in regions of confined GQDs. As the reduction process removes oxygen, formerly isolated sp^2 carbon atoms join together to form conjugated carbon rings, and regions that already contain large-area conjugated sp^2 carbon structures increase in size. The observed decreasing area of the peak at 2.3 eV with photoreduction suggests this peak emission is likely due to edge states or oxygen defects at the boundaries of the sp^3 region. The newly formed GQDs in rGO are ascribed to the increasing PL at 2.7, 1.80, and 1.55 eV peaks.

DFT studies by Sk *et al.* [21] support that the band gap energy of GQDs changes with respect to its size and found that GQDs $\sim$1.3 nm in mean diameter create Frenkel exciton states $\sim$2.7 eV, while slightly larger 2 nm GQDs emit $\sim$1.8 eV. Here, rGO contains an ensemble of GQDs of various sizes separated by oxygenated regions. Reduction removes oxygen, gradually increasing the GQD size, evidenced by the increased PL in rGO at 1.55 and 1.80 eV.

Figure 5(a) (inset) contains a qualitative depiction of the bands and energy levels in GO. The optical response of graphene is determined by the π and π^* states, which lie between the σ-σ^* gap in GO [45,57]. Oxygen functional groups break the symmetry of the pristine graphene lattice, resulting in localized defect states that exist in the π-π^* gap. Since the gap between σ states is $\gg$2.4 eV, this emission is suggested as the n-σ transition (dashed purple arrow). In both GO and rGO, emission at 2.7 eV dominates the PL spectra, which was shown to result from π states in isolated sp^2 domains (gray dashed arrow) [42]. Emission at lower energies comes from a broad range of GQD states and the local disorder states.

Figure 5(b) shows the degenerate TA response of the samples at 1.8 and 2.5 eV, respectively. At 1.8 eV, we observe a saturable absorption signal containing a long component that slowly goes away with reduction. At 2.5 eV, we see a reverse saturable absorption response, which decays extremely quickly in all samples. A similar transition has been previously observed by Bhattacharya *et al.* [58], who saw that a sign flip in the pump-probe response occurred at $\sim$2.3 eV. Since the most reduced samples have the largest reverse saturable absorption response, we can rule out excited-state absorption from oxygen groups as the cause of the sign flip. We attribute this sign change to absorption from the interband transition in graphene, which has been previously documented to exhibit a sign flip for high pump fluences at this energy [52,59]. We do not see a change in sign when probing the oxygen states at 1.8 eV, further confirming the sp^2 nature of the peak labeled GQD_2.

Figure 5(c) shows the 1.2 eV probe energy pump fluence dependence. At low pump fluences, the TA response of all samples exhibits a linear dependence on the pump fluence. Above incident photon flux of $\sim 4 \times 10^{12}$ photon/cm^2, a sublinear trend is observed that is fit to the Eq. (2) hot-electron cooling model TA response. The nonlinear saturation effect fits the expected nonlinear Fermi-Dirac filling factor. Notably, the more oxidized rGO_1 and rGO_2 samples have the most nearly linear behaviors, consistent with the expected smaller confined sp^2 sublattice regions. In Fig. S5 in the Supplemental Material [35], the raw transient transmittance ΔT ($t = 0.3$ ps) for 1.2 eV probe energy is plotted at each stage of photoreduction vs photon flux. Figure S5 in the Supplemental Material [35] shows the rGO_{2-3} photoreduction stages give the largest transient transmittance response, consistent with our prior conclusion that moderate reduction is optimal to recover graphenelike photophysics in rGO. Figure 5(c) (inset) shows the pump power dependence for the differential transmission at 1.8 eV pump and probe. This trend follows the monotonic increase with photoreduction also seen with the absorption spectra amplitude in Fig. 1(c) at 1.8 eV.

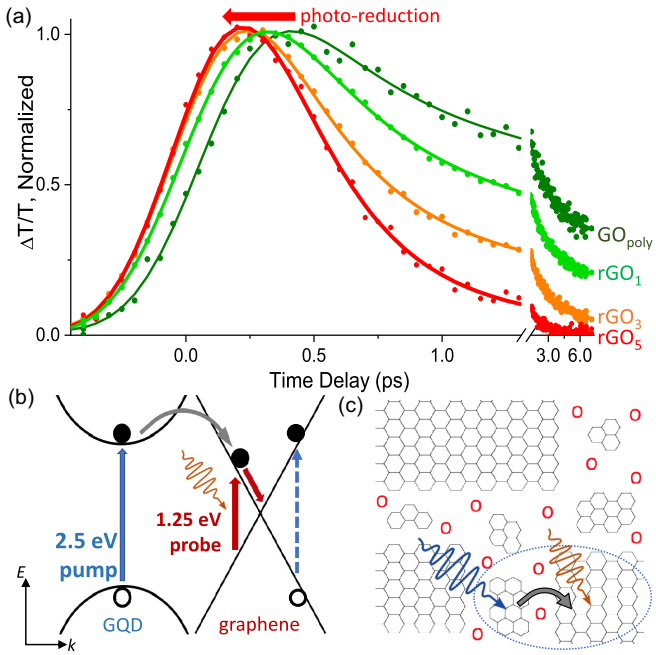

FIG. 6. (a) The normalized transient absorption kinetics fitted show a ∼170 fs delayed rise time for graphene oxide (GO) that systematically accelerates with successive photoreduction. (b) The observed rise time suggests a delayed energy transfer relationship between the 2.5 eV pump of graphene quantum dot (GQD) localized states and the 1.2 eV probe of the graphene states. (c) Illustration of reduced GO (rGO) lattice shows energy or charge transfer processes from confined GQDs to larger sp^2 graphenelike regions.

The pump energy dependence gives us insight into how the probe response changes with lattice temperature. At low pump powers, the 1.2 eV probe response has the same magnitude for all samples, suggesting that even oxidized samples have large regions of graphenelike sp^2 hybridization. The 1.8 eV data remain linear overall pump fluences but have a large dependence on the amount of reduction. While the 1.2 eV data probe graphenelike states, the 1.8 eV data primarily probe the confined GQD_2 states that lead to longer lifetimes and a strong dependence on photoreduction. The size and population of these GQD states depend heavily on the oxygen content. As shown in Fig. 5(c) (inset), reduction increases the transient response, which suggests that reduction increases the population of sp^2 GQD_2 states that absorb at 1.8 eV. This trend matches the increase in PL seen at 1.8 eV after photoreduction.

D. Ultrafast energy transfer dynamics in reduced graphene oxide

Using nondegenerate TA spectroscopy, we can excite molecularlike GQDs at high energies and probe the energy or electron transfer rate to graphene at lower-energy states. Figure 6(a) shows the normalized TA relaxation at 2.5 eV pump and 1.2 eV probe near time zero, which shows a clear delayed rise in the most oxidized samples. Conversely, the most reduced samples show a rise limited by the laser cross-correlation. This delayed rising kinetic edge is indicative of an acceptor-donor electron relationship. Charge transfer has been previously documented in GO, where photoexcited charges on a different molecular species are transferred to GO [60–62]. Alternatively, energy-transfer mechanisms between 2D semiconductors and graphene heterostructures have also been well documented [63–66].

In a model for energy transfer, the rapid electronic thermalization on the graphenelike lattice is delayed from the electronic coupling to a GQD site. At the 2.5 eV pump energies employed, the absorption line shape analysis in Fig. 3 shows no evidence of localized excitation (Gaussian) peaks directly that would suggest direct excitation of localized GQD states. Instead, this is more supportive of an energy transfer argument. Here, a delocalized excitation between GQD and rGO graphenelike states results in a delayed thermalization to the lower graphene energies [as illustrated in Figs. 6(b) and 6(c)]. Li *et al.* [67] recently measured the electron charge transfer rate between electron donor nanoparticles and GO at ∼1.0 ps. Such long time scales for stepwise acceptor-donor charge transfers suggest that our much shorter ∼0.17 ps delayed rise seen in Fig. 6(a) is instead more consistent with a delayed energy transfer to graphenelike regions of GO.

Figure 6(b) illustrates charge and energy transfer between localized GQDs state and graphene regions and suggests internal energy transfer may be responsible for the observed delayed rise. Carriers photoexcited in the confined GQD states are localized owing to the surrounding oxygen functional groups. In GO, the large density of oxygenated regions may result in weaker coupling between confined GQDs and graphene sublattice regions, enabling observation of a delayed rise. In the photoreduced samples, carriers excited into sp^2 GQD states may be closer to graphene regions, so the delayed energy transfer is no longer observed.

Electron-electron thermalization times in graphene are known to be remarkably fast (<10 fs), as such a graphenelike lattice should not have a delayed rise [68]. A delayed rise implies an energy or electron transfer process from higher-energy localized (GQD) states to graphenelike regions of rGO, as depicted in Fig. 6(b). The likely involvement of GQDs is evidenced by our pump-energy-dependent rising TA dynamics. Specifically, the rise effect was dominant using a 2.6 eV pump, much weaker using a 2.5 eV pump in Fig. 2(b), and is not observed at all with a degenerate 1.8 eV pump and probe in Fig. 1(d). This suggests that the excitation energy in GO samples preferentially localizes on the more prevalent smaller GQD states (at higher energy) before it thermalizes with neighboring graphenelike states. Similar energy transfer and localization pathways have been previously observed between 2D semiconducting materials and graphene [63–66]. In this model for energy transfer, the rapid electronic thermalization on the graphenelike lattice is delayed from the electronic coupling to a GQD site.

Lastly, Fig. 6 suggests evidence of acceptor-donor energy or electron transfer processes within a rGO lattice. Our GO begins with ∼44% oxygen content; these oxygen functional groups interrupt the delocalized π orbitals and prohibit hopping between carbon sites. Reduction removes oxygen, which decreases the mean distance from a confined GQD donor and graphenelike sp^2 sublattice region. Such changes to the effective percolation network of the sp^2 sublattice have previously been shown to also increase GO carrier mobility and conduc-

tivity [69–71]. The longer dynamics in GO may be caused by excited carriers becoming more isolated by the larger oxygenated regions shown in Fig. 6(c), which can restrict the relaxation pathways available. As rGO is further reduced, the removal of oxygen can recover larger-area graphenelike domains. These domains still decay more quickly than pristine graphene owing to lattice disorder induced by the photothermal reduction. Here, ml-graphenelike recovery was best observed for a narrow range of moderate photoreduction times ($rGO_{2–3}$) where sufficient oxygen is removed, but the photoinduced lattice disorder has not yet accelerated electronic cooling appreciably.

V. CONCLUSIONS

The highly variable composition of the quasiamorphous GO 2D lattice makes a systematic comparison against ml-graphene a challenge. To help overcome this challenge, GO is suspended in a polymeric network scaffold where five successive photoreductions ($rGO_{1–5}$) were possible without any evidence of interlayer aggregation. Ultimately, this yielded optical-quality rGO films with an absorption line shape that fits ml-graphene Fano resonance line shape parameters. Likewise, this stepwise photoreduction accelerates the hot-electron relaxation kinetics monotonically over each of the variable probe energy windows studied from 1.2 to 2.5 eV. At intermediate photoreduction times ($rGO_{2–3}$), Fig. 4 shows that a hot-electron cooling model of disorder-assisted SC matches the $\tau_{SC} = 3.1$ ps hot-electron cooling of ml-graphene. Figure 4(b) shows the recovery of ultrafast hot-electron relaxation rates similar to ml-graphene in moderately reduced samples ($rGO_{1–3}$), suggesting a largely uninterrupted sp^2 bonded network analogous to graphene.

Graphenes electronic cooling rate τ_{SC}^{-1} scales with $\frac{\lambda}{k_F l} T_l$ near room temperature [51]. Applying this model to GO materials, stepwise photoreduction is expected to primarily modulate the mean-free electronic scattering length $k_F l$. GO photoreduction initially seems to increase $k_F l$, for instance, by removing rogue oxygen-group edge states from otherwise well-formed graphenelike regions. At this point, Fig. 4 suggests that films of rGO are the most graphenelike, exhibiting both the largest transient transmittance and a slower electronic cooling rate that matches ml-graphene. In Fig. 4(b), subsequent photoreduction increases the hot-electron cooling rate $\sim 10\times$ for the most reduced rGO_5 sample. The SC model in Eq. (3) would then suggest a corresponding $\sim 10\times$ smaller $k_F l$ once the photoinduced point defects are sufficiently dense on the rGO lattice.

Predictably, after extreme photoreduction, the optical properties of rGO deviate more strongly from graphene. Owing to increasing local disorder and broken lattice symmetry, extreme photothermal reduction yields hot-electron cooling rates in Fig. 4(b) that are faster than ml-graphene measured under the same conditions. Specifically, photoreduction accelerates the extracted hot-electron cooling rate, revealing how photodamage induces local disorder to mediate faster hot-electron cooling. At longer time scales, GO exhibits a slower decay response than graphene owing to many isolated GQD regions and oxygenated-edge trap states. The prevalence of isolated GQD regions and oxygenated-edge trap states each creates further bottlenecks of electronic relaxation that slow the effective relaxation. Fortunately, we find these long lifetimes of rGO are no longer observed <1.3 eV optical excitations, as there are no discernible GQD sublattice states large enough to create resonance at these energies. Collectively, these results show many of the desirable optoelectronics properties of 2D graphene can be replicated using selectively reduced GO suspended in a three-dimensional bulk polymeric network. This paper lends itself to large-scale processing of rGO thin films and applications in high-speed optoelectronics and photonic switching applications.

The data that support the findings of this paper are available from the corresponding author upon reasonable request.

ACKNOWLEDGMENTS

This paper is based upon work supported by the Office of the Under Secretary of Defense for Research and Engineering under Award No. FA9550-22-1-0276 and the DEVCOM Army Research Laboratory Award No. W56HZV-18-C-0015.

[1] G. Yang, L. Li, W. B. Lee, and M. C. Ng, Sci. Technol. Adv. Mater. **19**, 613 (2018).
[2] K. A. Mkhoyan, A. W. Contryman, J. Silcox, D. A. Stewart, G. Eda, C. Mattevi, S. Miller, and M. Chhowalla, Nano Lett. **9**, 1058 (2009).
[3] T. Mueller, F. Xia, and P. Avouris, Nat. Photonics **4**, 297 (2010).
[4] M. C. Lemme, F. H. L. Koppens, A. L. Falk, M. S. Rudner, H. Park, L. S. Levitov, and C. M. Marcus, Nano Lett. **11**, 4134 (2011).
[5] F. Bonaccorso, Z. Sun, T. Hasan, and A. C. Ferrari, Nat. Photonics **4**, 611 (2010).
[6] J. Yan, M.-H. Kim, J. A. Elle, A. B. Sushkov, G. S. Jenkins, H. M. Milchberg, M. S. Fuhrer, and H. D. Drew, Nat. Nanotechnol. **7**, 472 (2012).
[7] P. Blake, P. D. Brimicombe, R. R. Nair, T. J. Booth, D. Jiang, F. Schedin, L. A. Ponomarenko, S. V. Morozov, H. F. Gleeson, E. W. Hill *et al.*, Nano Lett. **8**, 1704 (2008).
[8] K. C. Fong and K. C. Schwab, Phys. Rev. X **2**, 031006 (2012).
[9] Y. Wu, C. F. Fu, Q. Huang, P. Zhang, P. Cui, J. Ran, J. Yang, and T. Xu, ACS Nano **15**, 7586 (2021).
[10] M. A. Velasco-Soto, S. A. Pérez-García, J. Alvarez-Quintana, Y. Cao, L. Nyborg, and L. Licea-Jiménez, Carbon **93**, 967 (2015).
[11] T. Ji, Y. Hua, M. Sun, and N. Ma, Carbon **54**, 412 (2013).
[12] H. Yang, H. Hu, Z. Ni, C. K. Poh, C. Cong, J. Lin, and T. Yu, Carbon **62**, 422 (2013).
[13] H. Shi, C. Wang, Z. Sun, Y. Zhou, K. Jin, S. A. T. Redfern, and G. Yang, Opt. Express **22**, 19375 (2014).
[14] Z. Liu, Y. Wang, X. Zhang, Y. Xu, Y. Chen, and J. Tian, Appl. Phys. Lett. **94**, 021902 (2009).
[15] M. Liu, X. Yin, E. Ulin-Avila, B. Geng, T. Zentgraf, L. Ju, F. Wang, and X. Zhang, Nature (London) **474**, 64 (2011).
[16] G. Xin, Y. Meng, Y. Ma, D. Ho, N. Kim, S. M. Cho, and H. Chae, Mater. Lett. **74**, 71 (2012).

[17] I. Boukhoubza, M. Khenfouch, M. Achehboune, B. M. Mothudi, I. Zorkani, and A. Jorio, J. Alloys Compd. **797**, 1320 (2019).

[18] Q. Zhang, H. Zheng, Z. Geng, S. Jiang, J. Ge, K. Fan, S. Duan, Y. Chen, X. Wang, and Y. Luo, J. Am. Chem. Soc. **135**, 12468 (2013).

[19] J. Wu, L. Jia, Y. Zhang, Y. Qu, B. Jia, and D. J. Moss, Adv. Mater. **33**, 1 (2021).

[20] O. Kozák, M. Sudolská, G. Pramanik, P. Cígler, M. Otyepka, and R. Zboil, Chem. Mater. **28**, 4085 (2016).

[21] M. A. Sk, A. Ananthanarayanan, L. Huang, K. H. Lim, and P. Chen, J. Mater. Chem. C **2**, 6954 (2014).

[22] R. Roy, R. Thapa, S. Chakrabarty, A. Jha, P. R. Midya, E. M. Kumar, and K. K. Chattopadhyay, Chem. Phys. Lett. **677**, 80 (2017).

[23] N. S. Suhaimin, M. F. R. Hanifah, M. Azhar, J. Jaafar, M. Aziz, A. F. Ismail, M. H. D. Othman, M. A. Rahman, F. Aziz, N. Yusof *et al.*, Mater. Chem. Phys. **278**, 125629 (2022).

[24] S. Zhu, Y. Song, J. Wang, H. Wan, Y. Zhang, Y. Ning, and B. Yang, Nano Today **13**, 10 (2017).

[25] S. Kaniyankandy, S. N. Achary, S. Rawalekar, and H. N. Ghosh, J. Phys. Chem. C **115**, 19110 (2011).

[26] R. Y. N. Gengler, D. S. Badali, D. Zhang, K. Dimos, K. Spyrou, D. Gournis, and R. J. D. Miller, Nat. Commun. **4**, 2560 (2013).

[27] X. Zhao, Z. B. Liu, W. B. Yan, Y. Wu, X. L. Zhang, Y. Chen, and J. G. Tian, Appl. Phys. Lett. **98**, 121905 (2011).

[28] D. Sebastian, A. Pallikkara, H. Bhatt, H. N. Ghosh, and K. Ramakrishnan, J. Phys. Chem. C **126**, 11182 (2022).

[29] J. H. Strait, H. Wang, S. Shivaraman, V. Shields, M. Spencer, and F. Rana, Nano Lett. **11**, 4902 (2011).

[30] H. Wang, J. H. Strait, P. A. George, S. Shivaraman, V. B. Shields, M. Chandrashekhar, J. Hwang, F. Rana, M. G. Spencer, C. S. Ruiz-Vargas *et al.*, Appl. Phys. Lett. **96**, 081917 (2010).

[31] M. W. Graham, S.-F. Shi, D. C. Ralph, J. Park, and P. L. McEuen, Nat. Phys. **9**, 103 (2013).

[32] A. Singh and S. Kumar, J. Phys. Chem. C **125**, 26583 (2021).

[33] I. Santoso, P. K. Gogoi, H. B. Su, H. Huang, Y. Lu, D. Qi, W. Chen, M. A. Majidi, Y. P. Feng, A. T. S. Wee *et al.*, Phys. Rev. B **84**, 081403(R) (2011).

[34] G. Yu, X. Liu, G. Xing, S. Chen, C. F. Ng, X. Wu, E. K. L. Yeow, W. S. Lew, and T. C. Sum, J. Phys. Chem. C **118**, 708 (2014).

[35] See Supplemental Material at http://link.aps.org/supplemental/10.1103/PhysRevB.107.224309 for further elaboration and details of experimental sample characterization and modeling of the transient optical conductivity and TA power dependence.

[36] R. Skomski, P. A. Dowben, M. Sky Driver, and J. A. Kelber, Mater. Horiz. **1**, 563 (2014).

[37] A. Bhaumik, A. Haque, M. Taufique, P. Karnati, R. Patel, M. Nath, and K. Ghosh, J. Mater. Sci. Eng. **6**, 364 (2017).

[38] A. H. Castro Neto, F. Guinea, N. M. R. Peres, K. S. Novoselov, and A. K. Geim, Rev. Mod. Phys. **81**, 109 (2009).

[39] L. Yang, J. Deslippe, C.-H. Park, M. L. Cohen, and S. G. Louie, Phys. Rev. Lett. **103**, 186802 (2009).

[40] K. F. Mak, C. H. Lui, and T. F. Heinz, Measurement of the thermal conductance of the graphene/SiO_2 interface, Appl. Phys. Lett. **97**, 221904 (2010).

[41] K. F. Mak, M. Y. Sfeir, Y. Wu, C. H. Lui, J. A. Misewich, and T. F. Heinz, Phys. Rev. Lett. **101**, 196405 (2008).

[42] C. T. Chien, S. S. Li, W. J. Lai, Y. C. Yeh, H. A. Chen, I. S. Chen, L. C. Chen, K. H. Chen, T. Nemoto, S. Isoda *et al.*, Angew. Chem., Int. Ed. **51**, 6662 (2012).

[43] P. Sehrawat, S. S. Islam, P. Mishra, and S. Ahmad, Sci. Rep. **8**, 3537 (2018).

[44] H. Yoon, Y. H. Chang, S. H. Song, E. S. Lee, S. H. Jin, C. Park, J. Lee, B. H. Kim, H. J. Kang, Y. H. Kim *et al.*, Adv. Mater. **28**, 5255 (2016).

[45] H. F. Liang, C. T. Smith, C. A. Mills, and S. R. Silva, J. Mater. Chem. C **3**, 12484 (2015).

[46] D. S. Sutar, G. Singh, and V. Divakar Botcha, Appl. Phys. Lett. **101**, 103103 (2012).

[47] A. C. Betz, S. H. Jhang, E. Pallecchi, R. Ferreira, G. Fève, J.-M. Berroir, and B. Plaçais, Nat. Phys. **9**, 109 (2013).

[48] F. Rana, J. H. Strait, H. Wang, and C. Manolatou, Phys. Rev. B **84**, 045437 (2011).

[49] L. Huang, G. V. Hartland, L.-Q. Chu, Luxmi, R. M. Feenstra, C. Lian, K. Tahy, and H. Xing, Nano Lett. **10**, 1308 (2010).

[50] J. C. W. Song, M. Y. Reizer, and L. S. Levitov, Phys. Rev. Lett. **109**, 106602 (2012).

[51] M. W. Graham, S.-F. Shi, Z. Wang, D. C. Ralph, J. Park, and P. L. McEuen, Nano Lett. **13**, 5497 (2013).

[52] L. M. Malard, K. Fai Mak, A. H. Castro Neto, N. M. R. Peres, and T. F. Heinz, New J. Phys. **15**, 015009 (2013).

[53] M. Breusing, C. Ropers, and T. Elsaesser, Phys. Rev. Lett. **102**, 086809 (2009).

[54] K. J. Tielrooij, J. C. W. Song, S. A. Jensen, A. Centeno, A. Pesquera, A. Zurutuza Elorza, M. Bonn, L. S. Levitov, and F. H. L. Koppens, Nat. Phys. **9**, 248 (2013).

[55] Z. Luo, P. Vora, E. J. Mele, A. T. C. Johnson, and J. M. Kikkawa, Appl. Phys. Lett. **94**, 111909 (2009).

[56] S. Wang, Y. Dong, C. He, Y. Gao, N. Jia, Z. Chen, and W. Song, RSC Adv. **7**, 53643 (2017).

[57] A. L. Exarhos, M. E. Turk, and J. M. Kikkawa, Nano Lett. **13**, 344 (2013).

[58] S. Bhattacharya, S. Raval, A. Ghorai, M. Karmakar, A. Dey, A. Midya, S. K. Ray, and P. K. Datta, Proceedings Volume 10672, Nanophotonics VII **10672**, (2018).

[59] R. Gatamov, A. Baydin, H. Krzyzanowska, and N. Tolk, Mater. Res. Express **7**, 095601 (2020).

[60] Y. Wang, Z. Ni, L. Liu, Y. Liu, C. Cong, T. Yu, X. Wang, D. Shen, and Z. Shen, ACS Nano **4**, 4074 (2010).

[61] F. Zheng, W. L. Xu, H. D. Jin, X. T. Hao, and K. P. Ghiggino, RSC Adv. **5**, 89515 (2015).

[62] X. Li, W. Zhang, W. Cui, Y. Sun, G. Jiang, Y. Zhang, H. Huang, and F. Dong, Appl. Catal. B **221**, 482 (2018).

[63] G. Froehlicher, E. Lorchat, and S. Berciaud, Phys. Rev. X **8**, 011007 (2018).

[64] M. Massicotte, P. Schmidt, F. Vialla, K. G. Schädler, A. Reserbat-Plantey, K. Watanabe, T. Taniguchi, K. J. Tielrooij, and F. H. L. Koppens, Nat. Nanotechnol. **11**, 42 (2016).

[65] C. Ferrante, G. D. Battista, L. E. P. López, G. Batignani, E. Lorchat, A. Virga, S. Berciaud, and T. Scopigno, Proc. Natl. Acad. Sci. USA **119**, e2119726119 (2022).

[66] K. T. Vogt, S. F. Shi, F. Wang, and M. W. Graham, J. Phys. Chem. C **124**, 15195 (2020).

[67] D. Li, X. He, L. Zhao, M. Jia, H. Li, S. Zhang, X. Zhang, J. Chen, Q. Jin, and J. Xu, Chem. A Eur. J. **29**, e202300025 (2023).

[68] S. Winnerl, M. Orlita, P. Plochocka, P. Kossacki, M. Potemski, T. Winzer, E. Malic, A. Knorr, M. Sprinkle, C. Berger *et al.*, Phys. Rev. Lett. **107**, 237401 (2011).

[69] V. B. Mohan, R. Brown, K. Jayaraman, and D. Bhattacharyya, Mater. Sci. Eng., B **193**, 49 (2015).

[70] Y. Wang, Y. Chen, S. D. Lacey, L. Xu, H. Xie, T. Li, V. A. Danner, and L. Hu, Mater. Today **21**, 186 (2018).

[71] B. A. Ruzicka, S. Wang, L. K. Werake, B. Weintrub, K. P. Loh, and H. Zhao, Phys. Rev. B **82**, 195414 (2010).